

Supplementary Materials For

Charge Carriers Modulate The Bonding Of Semiconductor Nanoparticle Dopants As Revealed By Time-Resolved X-Ray Spectroscopy

Asra Hassan [†], Xiaoyi Zhang [‡], Xiaohan Liu [†], Clare E. Rowland [§], Ali M. Jawaid [†], Soma Chattopadhyay [‡], Ahmet Gulec ^{||}, Armen Shamirian [†], Xiaobing Zuo [‡], Robert F. Klie ^{||}, Richard D. Schaller ^{§, ⊥}, Preston T. Snee ^{†*}

[†]Department of Chemistry, University of Illinois at Chicago, 845 W. Taylor Street, Chicago, Illinois 60607-7061, USA. [‡]X-ray Science Division, Argonne National Laboratory, Argonne, IL 60439, USA. [§]Department of Chemistry, Northwestern University, 2145 Sheridan Road, Evanston, Illinois, 60208-3113, USA. ^{||}Department of Physics, University of Illinois at Chicago, 845 W. Taylor Street, Chicago, Illinois 60607-7061, USA. [⊥]Center of Nanoscale Materials, Argonne National Laboratory, Argonne, IL 60439, USA.

Correspondence to: sneep@uic.edu

Index	Page
Experimental.	S2
Table S1. Multi-exponential fit parameters to time- and wavelength-resolved photoluminescence.	S3
Figure S1. Time-resolved oxidation and emission dynamics.	S3
Figure S2. XRD Spectrum of Cu ₄ :CdS NCs.	S4
Figure S3. TEM images of Cu ₄ :CdS NCs.	S5
Elemental Analysis Results	S6
Table S2. Elemental analysis results on the copper content of Cu ₄ :CdS NCs.	S6
Figure S4. Magnetic susceptibility measurement at variable temperatures.	S7
Figure S5. FTIR spectra reveal oleylamine surface ligands of Cu ₄ :CdS NCs.	S7
Figure S6. XPS spectra of neat and copper-doped CdS NCs.	S8
Static X-ray absorption measurement details.	S9
Table S3. Fit parameters obtained from modeling the data for Cu edge of copper doped NC.	S9
Figure S7. Copper K-edge XANES spectra of Cu ₄ :CdS samples before and after exposure to high intensity UV radiation.	S10
Figure S8. The effect of using different weight factors to generate the excited XANES spectrum.	S10

Figure S9. Demonstration of the linear power-dependency behavior of Cu oxidation kinetics	S11
Figure S10. Ground and excited state Cu-K EXAFS spectra.	S11
Figure S11. SAXS analysis reveals Cu ₄ :CdS size distribution.	S12
Additional DFT calculation details.	S13
Figure S12. Optimized local Cu-centered geometries of copper-doped CdS, ZnSe, InP, and InAs clusters in the ground singlet 1 st excited triplet states.	S14
Figure S13. The effect of charge-modulated dopant bonding observed in copper atoms at the surfaces.	S15
Figure S14. NTO orbital analysis of the 1 st excited state of an interior-doped InCd ₆₅ S ₆₆ (H ₂ CO ₂) ₁₈ cluster.	S16
Figure S15. Optimized local Cu-centered geometries of copper-doped CuCd ₆₅ Se ₄ S ₆₂ (H ₂ CO ₂) ₁₈ and CuCd ₆₅ O ₄ S ₆₂ (H ₂ CO ₂) ₁₈ clusters in the ground singlet 1 st excited triplet states.	S16
Figure S16. Z-clipped image of a copper-doped CuCd ₁₃₇ S ₁₃₈ (H ₂ CO ₂) ₂₅ model.	S17
References.	S17

Experimental

[N(Me₄)₂][Cu₄(SPh)₆] cluster synthesis. [N(Me₄)₂][Cu₄(SPh)₆] clusters were synthesized according to previously published protocols with slight modifications.¹⁻² The procedure is restated here for completeness. Into a one-neck round-bottom flask connected with a dripping funnel, 25 mL of triethylamine, 50 mL of methanol, and 10 g of benzenethiol (97 mmol) were added, and the solution was flushed with N₂ for 1 hr. After heating the solution to reflux, 8.0 g (33.1 mmol) Cu(NO₃)₂·3H₂O dissolved in 40 mL of methanol was added dropwise. The solution quickly turned yellow, the coloring of which remained throughout the process. Addition of the copper nitrate solution was stopped when the reaction vessel was saturated with yellow products, evaluated by the increasingly lower solubility of Cu(NO₃)₂. After the solution cooled to room temperature, 2.5 g (23 mmol) of tetramethylammonium chloride dissolved in methanol was added to the solution, which was layered with 2-propanol immediately. The solution was allowed to equilibrate overnight at room temperature under N₂. The product precipitated as yellow crystals, which were filtered, washed with cold acetone and ether, dried under vacuum, and stored in a glovebox. See reference 2 for characterization data.

Characterization.

Optical. UV/Vis absorbance spectra were taken using a Varian Cary 300 Bio UV/Vis spectrophotometer. Temperature-dependent photoluminescence spectra and dynamics were acquired using a 35 ps pulsed laser diode operating at 450 nm and 500 kHz repetition rate. The collected emission was directed to a 300 mm focal length grating spectrograph and either detected with a CCD for spectra or an avalanche photodiode for detection of a specific wavelength. Sample temperature control was afforded via a sample in vacuum, closed-cycle helium cryostat.

Wavelength (nm)	Amp.	τ (ps)	Amp.	τ (ns)	Amp.	τ (ns)	Amp.	τ (ns)
540	-	-	0.733	2.65 ± 0.06	0.190	35.5 ± 1.3	0.076	348 ± 8
550	-	-	0.699	3.46 ± 0.06	0.214	55.5 ± 1.3	0.087	428 ± 7
600	-	-	0.481	9.51 ± 0.10	0.317	118.1 ± 1.2	0.203	546 ± 3
650	-	-	0.375	17.06 ± 0.15	0.377	178.5 ± 1.3	0.248	695 ± 3
690	-	-	0.346	21.5 ± 0.2	0.377	210.9 ± 1.7	0.277	782 ± 3
700	-	-	0.335	21.6 ± 0.2	0.382	219.0 ± 1.7	0.283	814 ± 3
750	-	-	0.303	20.3 ± 0.3	0.369	225 ± 2	0.328	881 ± 4
800	-	-	0.304	20.1 ± 0.5	0.348	234 ± 4	0.347	954 ± 6
850	-	-	0.306	18.4 ± 0.9	0.336	223 ± 7	0.358	993 ± 11
900	-	-	0.343	16.1 ± 1.1	0.349	235 ± 7	0.308	1088 ± 11
TR-XAS	0.49 ± 0.07	160 ± 80	0.27 ± 0.04	11 ± 9	-	-	0.24 ± 0.04	1100 ± 500

Table S1

Multi-exponential fit parameters to time- and wavelength-resolved photoluminescence data shown in Fig. 5 of the main text. The amplitude uncertainties of the PL data are on the order of 0.1% and are not reported for clarity. The TR-XAS oxidation kinetic data shown in Fig. 5 were quantified by integrating the magnitude of the bleach signal at 8982 eV.

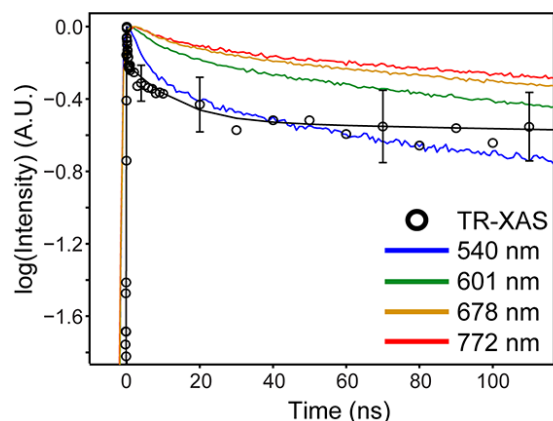


Figure S1. A log-linear plot of PL and oxidation kinetics at early times reveals the fast, ~ 160 ps oxidation kinetics that are absent in the emission data. Furthermore, the ~ 100 -200 ns emission

decay seen at all wavelengths is absent from the oxidation dynamics. Note these data are identical to those shown in Fig. 5 of the main text.

X-ray diffraction X-ray diffraction (XRD) studies were performed on a D8 Advance ECO Bruker XRD diffractometer using a graphite monochromator and a proportional detector. The power generator was operated at 40 kV and 20 mA.

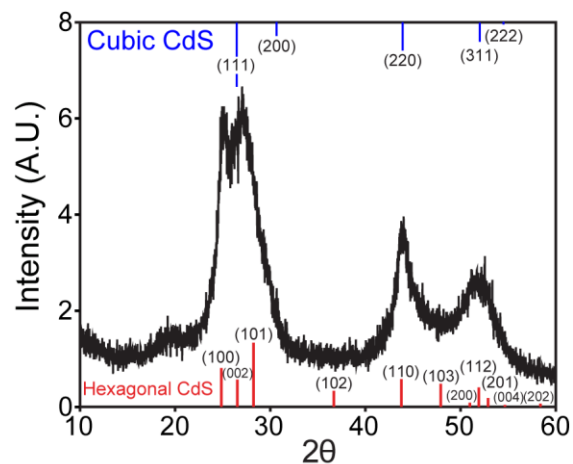


Figure S2. XRD shows a preeminent peak around bulk Wurtzite CdS (101) facet signal ($2\theta=27^\circ$) implying a Wurtzite structure or a Wurtzite dominating mix structure compared to the zinc blende (cubic) structure of $\text{Cu}_4\text{:CdS}$ NCs.

Electron Microscopy. Transmission Electron Microscopy (TEM) images were obtained on a JEOL JEMARM 200CF electron microscope operating at 200 kV with a cold field emission source for high spatial resolution with combination of imaging modes including high angle annular dark field (HAADF, see below) imaging with an inner collecting angle of 68 mrad and outer collecting angle of 230 mrad, annular bright field (ABF) imaging with an inner collecting angle of 11 mrad and outer collecting angle of 22 mrad. A probe side Cs-corrector was used to yield a probe size of approximately 0.078 nm. Under daily operating conditions, the third order aberrations remain stable for days while the second order aberrations were monitored and corrected as needed during the experiments. Other images shown below were obtained using a JEOL JEM-3010 operating at 300 keV. A 300 mesh gold grid was used for nanoparticle imaging. These data were used to verify the size of the NCs to validate the product yield vs. cluster seed mass data shown in Fig. 1B of the main text.

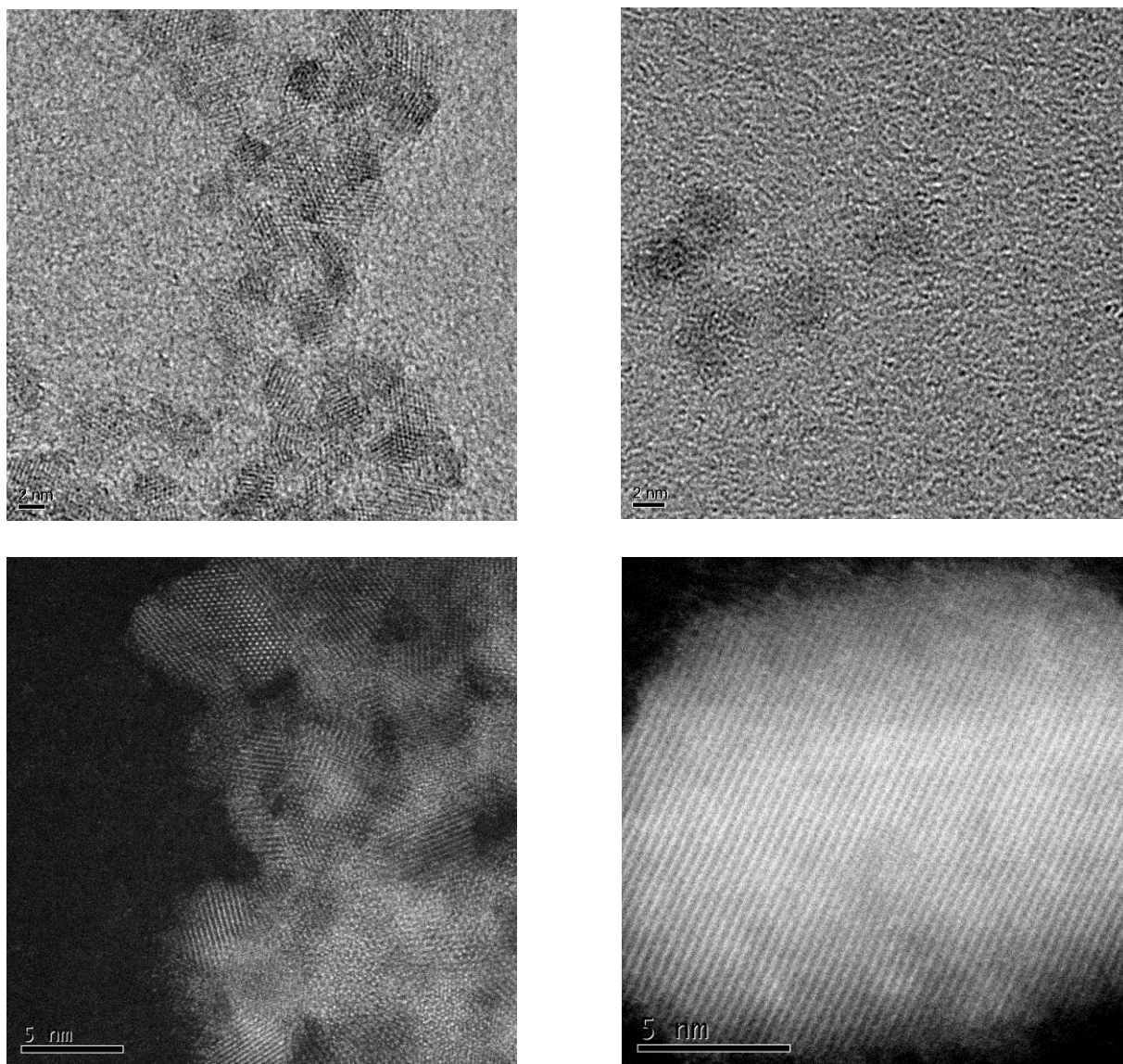


Figure S3. TEM micrographs of copper doped CdS NCs.

Elemental Analysis and Pyridine Cleaning. To characterize the elemental composition, several ~1g portions of the growth solution containing Cu₄:CdS NCs were processed with precipitation several times to remove the solvent (mostly octadecene), and were digested according to EPA method 3050B.³ Several blanks and other controls such as blanks spiked with copper and cadmium standards that reflected the estimated composition of the NCs were processed using the same protocol. Atomic absorption (AA) spectroscopy was performed using a PerkinElmer AAnalyst 200. Machine drift was tracked by bracketing every 10 measurements with calibration standards; if the standard was outside of 10% of its nominal value, the AA was recalibrated and the samples were re-analyzed.

Sample	Estimated Cu (ppm)	Recovered Cu (ppm)	% Incorporation
1	5.0	4.89 ± 0.06	97.8 ± 1.2 %
2	5.0	4.538 ± 0.008	90.76 ± 0.16 %
3	10.0	9.50 ± 0.05	95.0 ± 0.5 %
Pyridine-etched	10.0	8.67 ± 0.06	86.7 ± 0.6 %

Table S2

Results of elemental analysis for copper in Cu₄:CdS NCs.

Blank samples contained low levels of copper and cadmium, while the recoveries of cadmium and copper that were spiked into blank samples were within 90%. Various quantities of a freshly-prepared Cu₄:CdS NC sample were digested and diluted to create a sample with a concentration that was within the linear detection range of the flame AA. It was found that the amount of copper that was added in the form of clusters was recovered to 94.6 ± 0.4%, which supports the mechanism of cluster seeding. The amount of cadmium recovered was 80%, which is the same as the reaction yield. The Cd:Cu ratio was determined to be 188×, which is consistent with the size of the NCs given that each QD contains 4 copper ions.

It was found that attempting to digest too large a portion of growth solution resulted in less copper recovery (~50%), which was likely due to the formation of an organic layer that formed during the sample processing that was unremovable using the method. Furthermore, an older Cu₄:CdS sample (~1 yr) was also analyzed, which was found to contain significantly less copper likely due to leaching of the element out of the NC.

To ascertain the level of copper on the surface of the NCs, a sample was precipitated and washed with pyridine overnight. The sample was digested as above, and the copper content measured. The Cu content was reduced by ~9%, which is an indicator that some ions reside on the surface. This is somewhat less than expected based on the X-ray data; however, we cannot validate the efficiency of pyridine removal of copper specifically from an NC surface. Given the quality of the X-ray data, we conclude that most of the dopant ions reside on the NC surface.

SQUID. Magnetic susceptibility data were collected from 2 K to 300 K under magnetic fields of 1000 and 5000 G using a Quantum Design MPMS-XL SQUID magnetometer. Samples were pressed powders of the quantum dots sealed in a gel cap. Susceptibility was corrected for the diamagnetism of the sample holder and the diamagnetic response of the sample itself, estimated with a "molecular" formula of $\text{Cd}_{950}\text{S}_{950}\text{Cu}_4(\text{C}_{18}\text{H}_{37}\text{N})_{50}$, using Pascal's constants.⁴ The magnetic susceptibility at all temperatures (aside from the very lowest) is negative, indicating a dominant diamagnetic contribution to the susceptibility. The $[\text{Ar}]3d^9$ electronic configuration of $\text{Cu}(2+)$ is $S = 1/2$. As such, the susceptibility data suggest that the Cu ions contained in the NCs are in the diamagnetic $\text{Cu}(+1)$ oxidation state, in agreement with the XANES data.

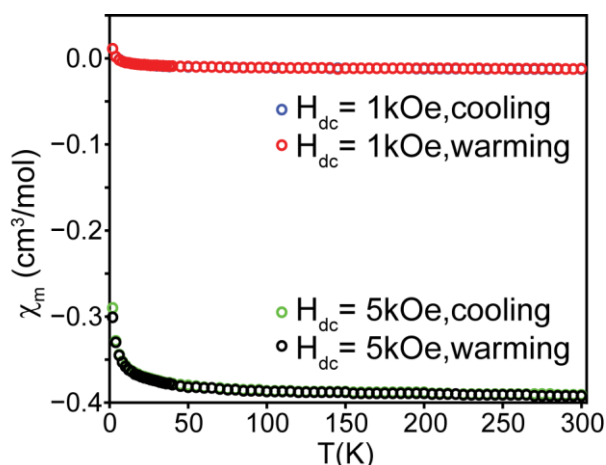


Figure S4. Variable temperature magnetic susceptibility data for the $\text{Cu}_4\text{:CdS}$ NCs under 1 and 5 kOe magnetic fields.

FTIR. Samples of $\text{Cu}_4\text{:CdS}$ NCs were processed *via* precipitation with a non-solvent (2-propanol and/or methanol) to remove excess octadecene and oleylamine to characterize their surface ligands using a Nicolet iS5 (Thermo Scientific) FTIR with an ATR sampler.

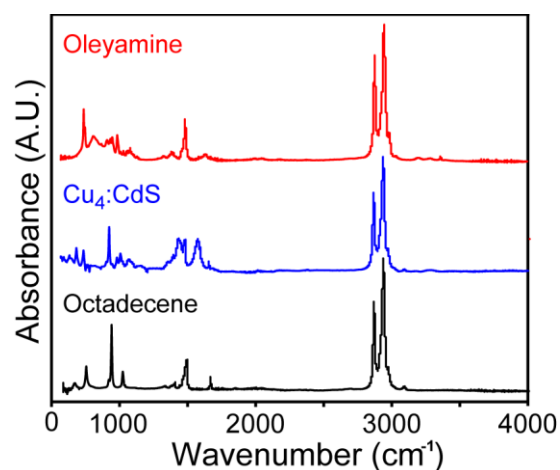


Figure S5. FTIR spectra of oleylamine, $\text{Cu}_4\text{:CdS}$ NCs, and 1-octadecene reveal that the spectrum of NC surface ligands is composed of ODE and oleylamine. However, the ODE features are

likely artefactual as the processing of samples to remove the organics proved highly problematic, and there is likely excess ODE present in the precipitate. As such, we are confident that the NCs are coated with oleylamine.

XPS. X-ray Photoelectron Spectroscopy (XPS) analyses were performed on a Kratos Axis 165 using a monochromatic Al K α source operating at 12 kV and 10 mA to produce an X-ray power of 120 W. Spectra were collected with a photoelectron takeoff angle of 90° from the sample surface plane, in energy steps of 0.1 eV, and a pass energy of 20 eV for all elements.

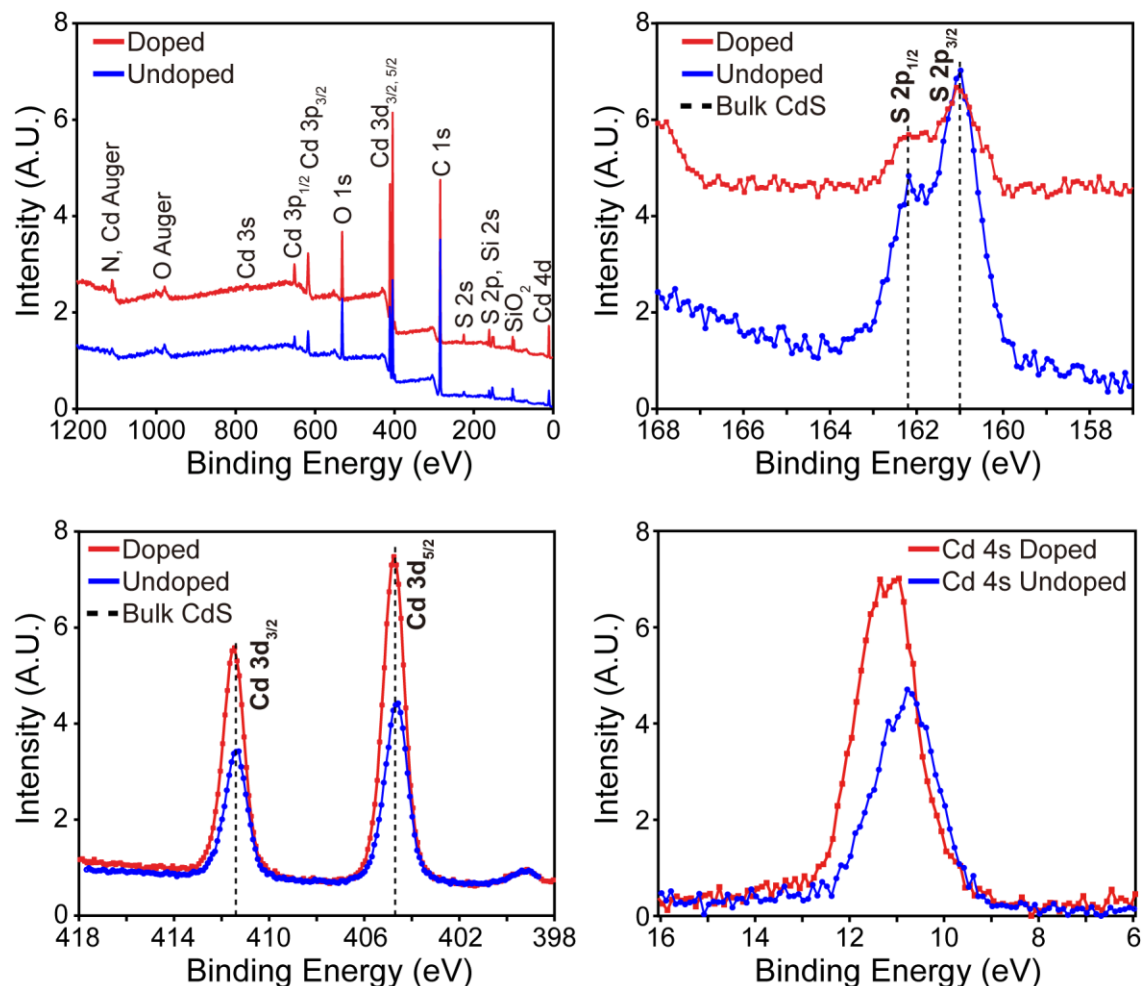


Figure S6. XPS spectra of neat and copper-doped CdS NCs. A comparison of the valence Cd-4s reveal a slight 0.1~0.2 eV blue shift, which could be explained by p-doping of the semiconductor hosts by the Cu guest ions.

Static X-ray Absorption. X-ray Absorption Near-Edge and Extended X-ray Absorption Fine Structure Spectroscopy (XANES and EXAFS) measurements at the Cu K-edge (8979 eV) were carried out at the Advanced Photon Source at Argonne National Laboratory to study the local environment of Cu dopants before and after illumination with strong UV light (Norland Opticure LED 200). The data in Figs. 2A and S7 were taken at beamline 10-ID-B, where Cu doped CdS samples dissolved in 1-octadecene were loaded into 0.5 mL circular safe-lock plastic Eppendorf tubes with a wall thickness of 700 μm . The absorption of the walls is minimal (0.392 at Cu K-edge); thus, it does not affect the Cu-edge absorption energy. All measurements were performed at room temperature at a 45° orientation to the beam. X-ray absorption measurements were collected in fluorescence mode using a four-element Vortex 411 solid-state fluorescence detector. The step size across the edge was 0.25 eV, and the measurement time was set to 2 s per point. XANES scans covered ~ 250 eV below copper's K-edge energy (8979 eV) and up to 300 eV above the Cu edge. EXAFS scans started from ~ 250 eV below to 650 eV above the Cu edge. A typical scan took about 20 min with data in higher k-space taken with a step size of $k = 0.05 \text{ \AA}^{-1}$ and measurement time of 4 s per step. The energy resolution of the monochromator is 0.25 eV. The position of the X-ray beam was moved between each scan to minimize sample degradation. Reference samples were spread over Kapton tape and subsequently stacked together such that the thickness (x) of the samples corresponded to $\Delta\mu x = 0.5$, where $\Delta\mu$ is the edge step of the absorption coefficient at the Cu K-edge energy. Cu_2S standard was measured in a transmission geometry using a quick scan mode with the monochromator measuring energy on the fly using step sizes of 0.3 eV and a measurement time of 0.1 s per step. Several scans were merged to obtain better statistics. A copper metal foil scan was simultaneously measured between the standard and NC sample using a reference ion chamber to calibrate the energy scale. These measurements used a reference detector composed of 70% He/30% N_2 and a transmission reference of 100% N_2 . All measurements used an incident X-ray spot size of $500 \times 500 \mu\text{m}$.

All other static X-ray absorption data were obtained at beamline 11-ID-D, including the EXAFS data shown in Fig. 2A inset. The following set of parameters were used in fitting these data.

Edge	Paths	Bond length (\AA)	Coordination Number	Debye-Waller Factor (\AA^2)	Energy Shift ΔE (eV)
R=1.0 – 2.2 \AA k= 2.0 – 12.5 \AA^{-1}	Cu-S	2.177 ± 0.004	1.6 ± 0.1	0.0049 ± 0.0005	4.7 ± 0.8

Table S3

List of fit parameters obtained from modeling the data for Cu edge of copper doped NC samples shown in Fig. 2A inset.

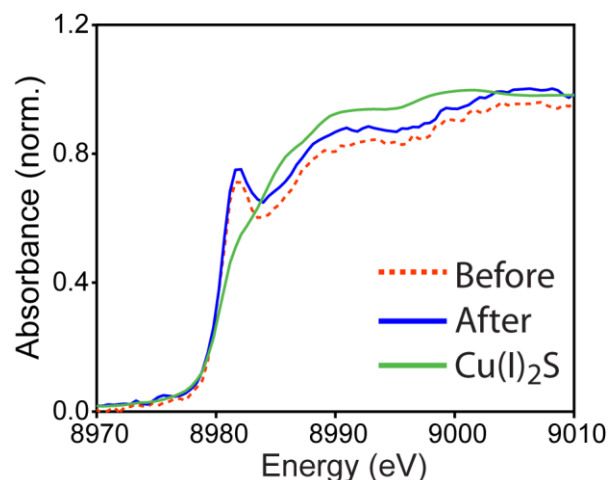


Figure S7. Copper K-edge XANES spectra of Cu₄: CdS samples before and after long-time exposure to high intensity UV radiation does not indicate dopant oxidation as was observed in Cu₄: CdSe in our previous report.² The photoluminescence was similarly found to be insensitive to significant exposure to UV excitation.

Time-resolved X-ray Absorption.

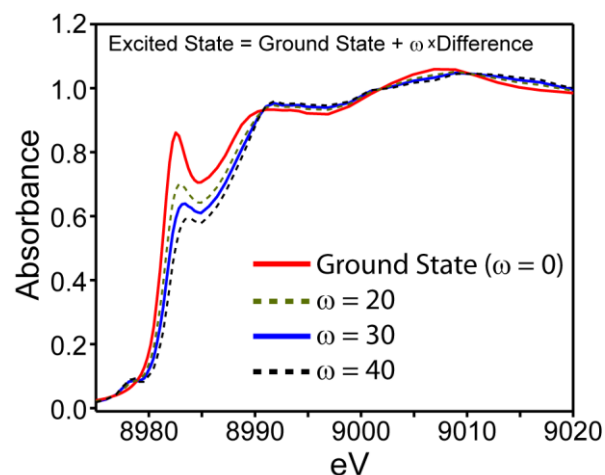


Figure S8. The excited state spectra shown in Fig. 2C of the main text were created by adding an increasing weight (ω) of the difference to the ground state spectrum. Shown here is the effect of using weighting factors of 20 \times , 30 \times , and 40 \times . Overall, there are no differences in the data that would alter the interpretation of the excited XANES spectrum as corresponding to Cu(2+) with a pre-edge feature observed at 8978 eV. Note that a factor of $\omega=20\times$ was used in the data presented in the main text.

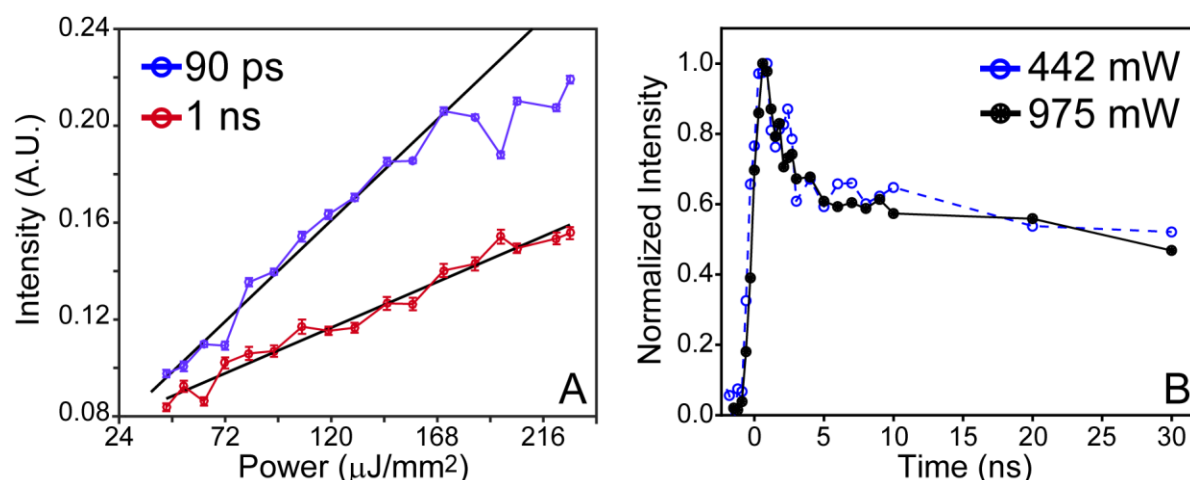


Figure S9. (a) The magnitude of the 8982 eV bleach vs. laser power at 90 ps and 1 ns delay times reveal linear power-dependent behavior, which indicates that non-linear effects such as multiphoton absorption to generate biexciton states and dynamics are not interfering with the data. (b) Power dependent Cu oxidation kinetics as measured by the normalized magnitude of the 8982 eV XANES bleach *versus* laser power demonstrate that single exciton dynamics are observed in this study.

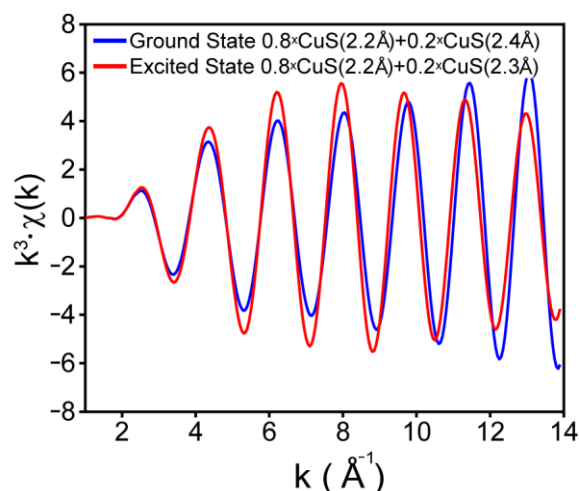


Figure S10. A simulated spectrum of the excited state Cu-K EXAFS (red line) has a smaller oscillation period in the k range of 3 \AA^{-1} to 9.4 \AA^{-1} compared to the ground state (blue line). However, this is the result of interference between two scattering signals as this simulation is composed of 80% amplitude from a 2.2 \AA Cu-S bond and 20% from a 2.3 \AA Cu-S bond, while the ground state is generated from a composition of 80% amplitude from a 2.2 \AA Cu-S bond and 20% from a 2.4 \AA Cu-S bond. These simulations reproduce the data shown in Fig. 4B, and is consistent with the fact that there are surface-bound dopant ions and interior species.

SAXS. Small Angle X-ray Scattering (SAXS) analysis were performed at the Argonne National Laboratory Advanced Photon Source Beamline 12-ID-B beamline to study the size distribution of the CdS:Cu₄ NCs suspended in 1-octadecene with a concentration of 0.1 mmol/L, using 14 keV X-ray energy. The SAXS data were collected with a Pilatus 2M detector and the cutoff energy was set to 10 keV to eliminate possible fluorescence background. The beam size of $0.05 \times 0.2 \text{ mm}^2$ and an exposure time of $\sim 1 \text{ s}$ were used for the measurements. The data were fully corrected, reduced to intensity versus scattering vector (q) profiles, and background subtracted with the Irena software package integrated in Igor Pro.⁵ These data were used to augment our estimation of NC size via absorption measurements.

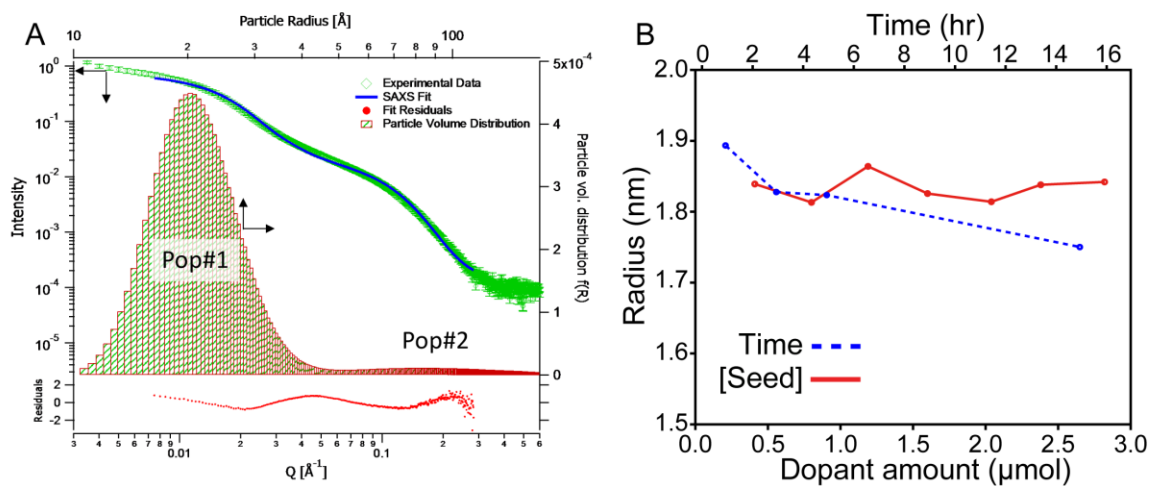


Figure S11. (a) The SAXS data (green) and fitting for particle size distribution (red bar). Two-particle size populations were found, both of which are assumed to following LogNorm distribution. They are labeled as Pop#1 and Pop#2, which arise from SAXS peaks around q of $\sim 0.06\text{--}0.3 \text{ \AA}^{-1}$ and $\sim 0.006\text{--}0.03 \text{ \AA}^{-1}$, respectively. Pop#1 is the major population and the average radius is $19 \pm 5 \text{ \AA}$. Pop#2 is a minor population and the average radius is $61 \pm 23 \text{ \AA}$. (b) The NC size vs. cluster seed mass and growth time was also studied using SAXS, which revealed that the synthetic method does not generate a wide size distribution of nanomaterials.

DFT Methods: Copper dopant calculations. For most clusters examined in this study, namely $\text{CuCd}_{32}\text{S}_{33}(\text{H}_4\text{C}_2\text{O}_2)_9$, $\text{CuCd}_{65}\text{S}_{66}(\text{H}_2\text{CO}_2)_{18}$, $\text{CuCd}_{113}\text{S}_{114}(\text{H}_2\text{CO}_2)_{18}$, NBO 6.0 analyses demonstrated that copper does not bond to any of the host matrices in the ground state and is oxidized $\sim +0.7$ units of charge. In 1st excited state, copper is oxidized by an additional $\sim +0.4$ units of charge and formally bonds to one or more nearby sulfur atom(s). The electronic configurations of the 1st excited states of all these copper-doped semiconductor systems were found to be triplet, which allowed for the optimization of the excited state geometries. NBO analysis of the excited state at their optimized geometries revealed that copper oxidation increased as shown in Fig. S12, and has bonds to the nearest two sulfur atoms.

Type II copper dopants. The paradigms discussed above did not apply to the case of “type-II” surface doping found in the largest $\text{CuCd}_{137}\text{S}_{138}(\text{H}_2\text{CO}_2)_{25}$ cluster employed in this study. This model is shown in Fig. 3C and Fig. S13 below. As discussed in the main text, the excited state of this configuration was found to involve oxidation of a surface-bound sulfur site. The copper center is hardly perturbed as its natural charge does not significantly increase, there is minimal redistribution of the coordination sphere as shown in Fig. S13, and no subsequent redistribution of the bonding of the copper dopant was found to occur.

Indium dopant calculations. The indium-doped $\text{InCd}_{65}\text{S}_{66}(\text{H}_2\text{CO}_2)_{18}$ cluster was simulated with a net +1 unit of positive charge to maintain a singlet ground state. Data from these calculations are shown in Fig. S14.

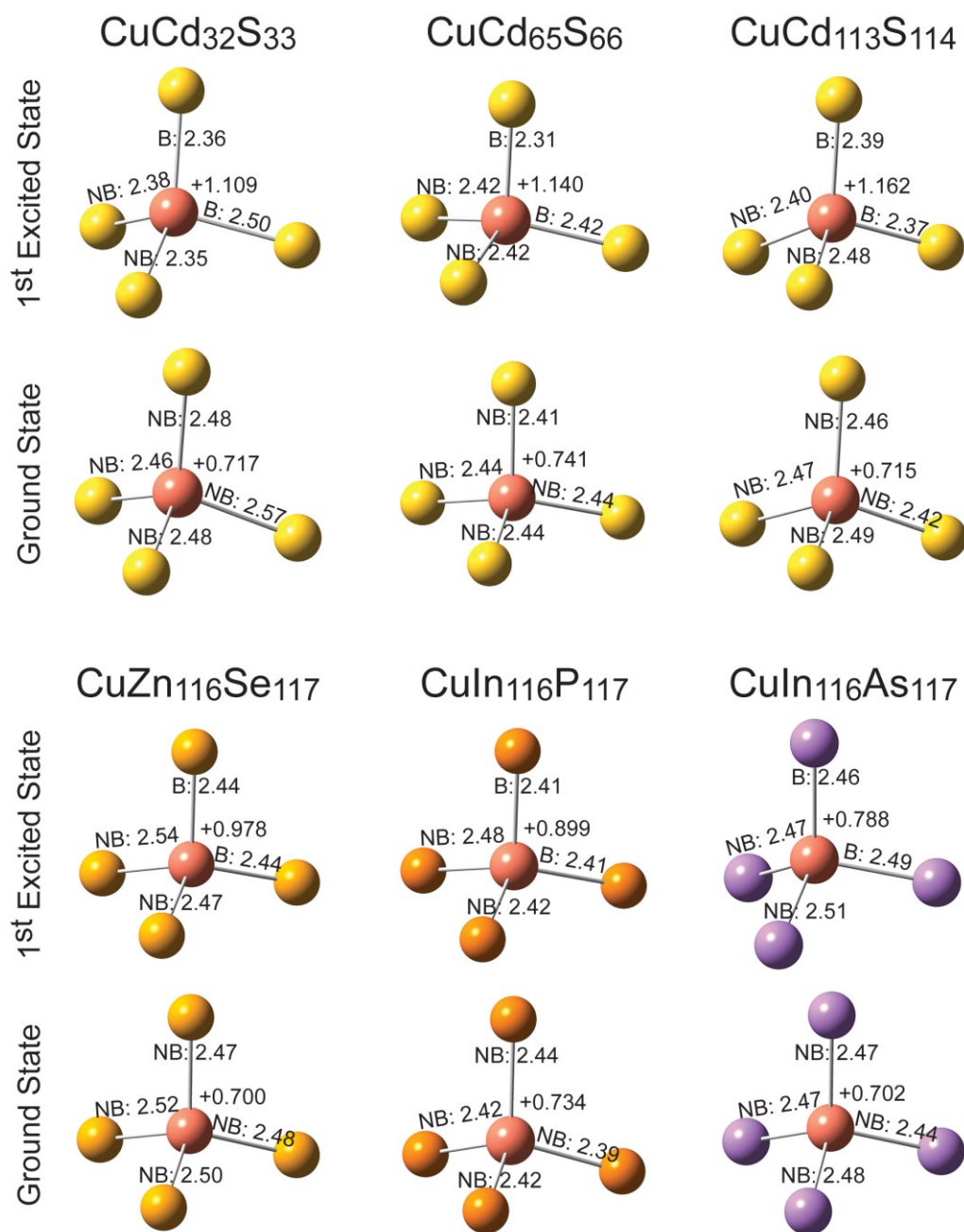


Figure S12. Optimized local Cu-centered geometries of copper-doped CdS, ZnSe, InP, and InAs clusters in the ground singlet 1st excited triplet states. The magnitude of bond rearrangement correlates with the degree of oxidation of the Cu dopant as indicated. The bond rearrangement is also proportional to the energy of the valence band, where shallow HOMO levels in the neat semiconductor (InAs, and InP to a lesser extent) result in less oxidation and bond rearrangement in the copper-doped cluster. NB: not bonded. B: single bond, although NBO analysis consistently finds occupancy of antibonding orbitals in all cases shown above.

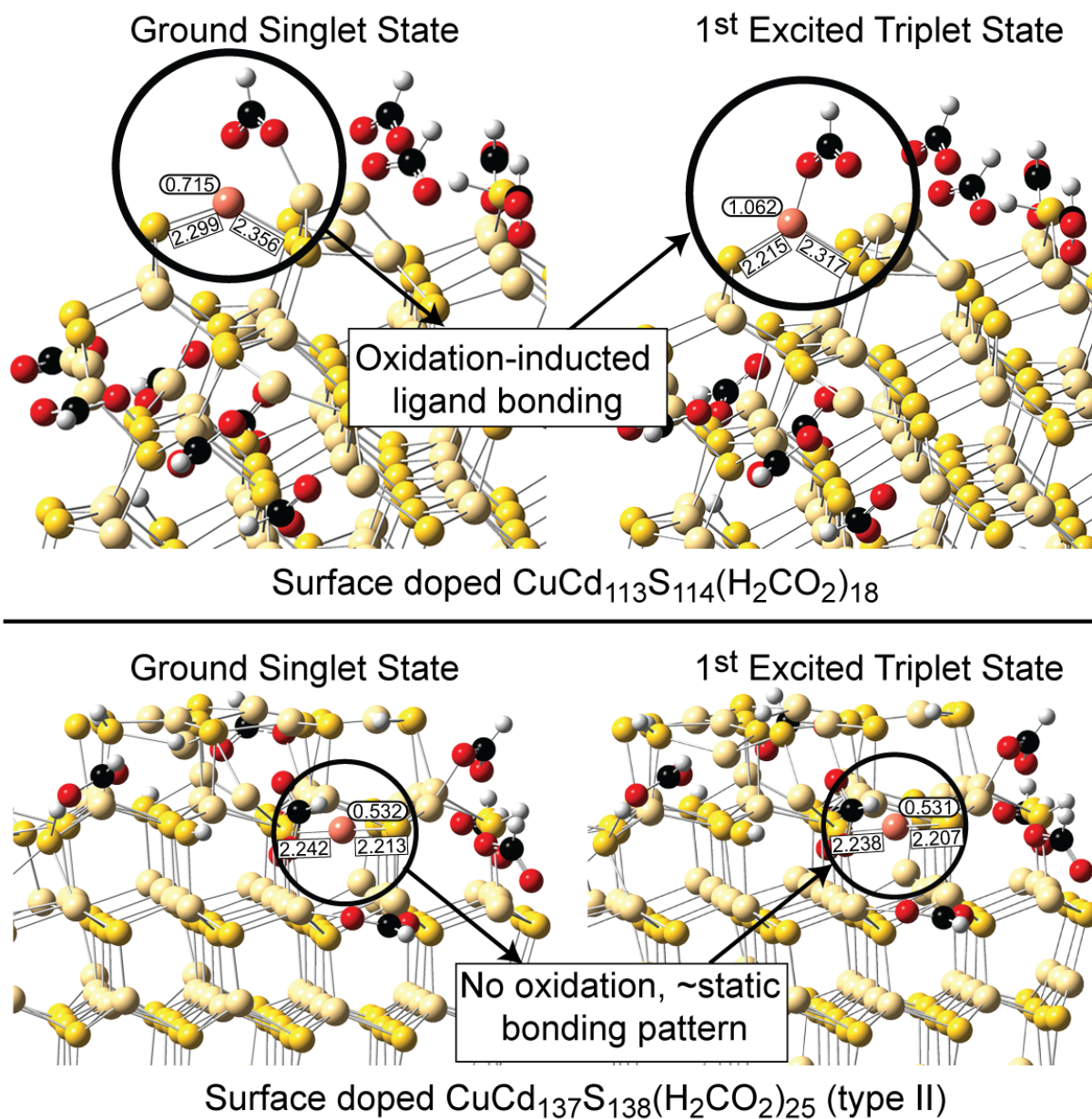


Figure S13. The effect of charge-modulated dopant bonding observed in copper atoms at the surfaces of smaller clusters. As shown here, oxidation of the surface-bound copper in $\text{CuCd}_{113}\text{S}_{114}(\text{H}_2\text{CO}_2)_{18}$ instigates bonding to a nearby ligand. For a type-II dopant found on the surface of the larger $\text{CuCd}_{137}\text{S}_{138}(\text{H}_2\text{CO}_2)_{25}$ cluster, there is minimal rearrangement of the coordination sphere due to the lack of significant oxidation of the dopant in the excited state. Note that the hole is localized on a nearby S-site as shown in Fig. 3C of the main text. Squares represents Cu-S distances, ovals convey the partial charge from NBO analysis.

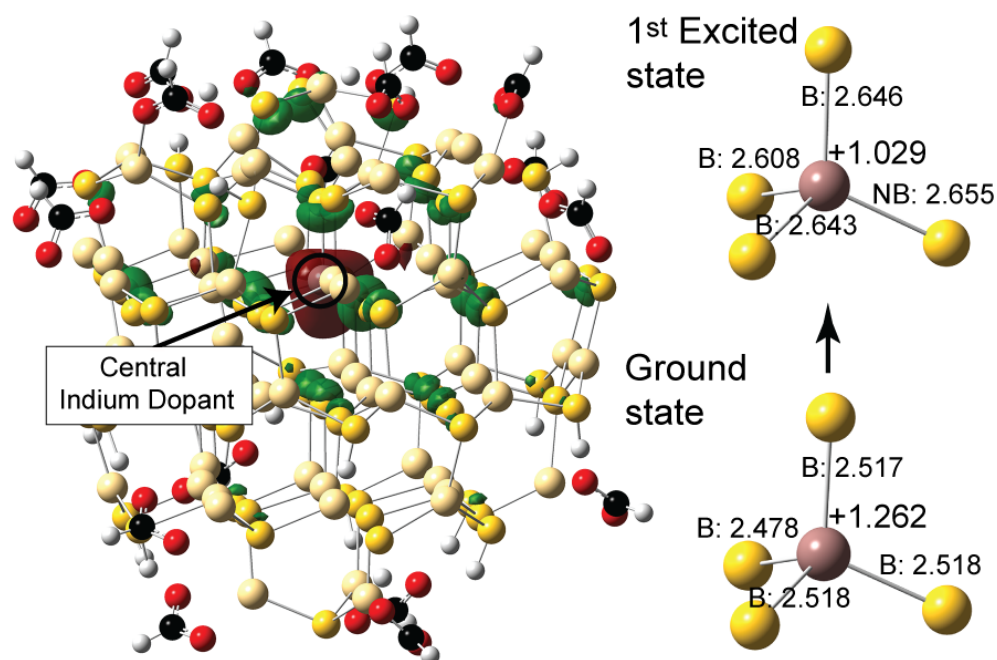


Figure S14. Natural Transition Orbital (NTO) orbital analysis of the 1st excited state of an interior-doped $\text{InCd}_{65}\text{S}_{66}(\text{H}_2\text{CO}_2)_{18}$ cluster demonstrates the addition of electron density on the In dopant in the excited state. The optimized geometry of the 1st excited state displays longer In-S bonds, while NBO analysis dictates that one of the bonds is broken while the remaining gain additional charge density in antibonding orbitals. NB: not bonded. B: single bond.

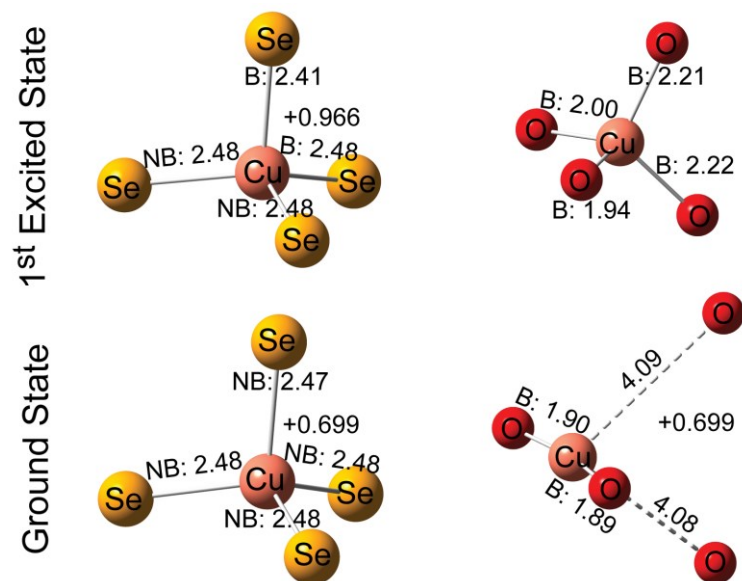


Figure S15. Optimized local Cu-centered geometries of copper-doped $\text{CuCd}_{65}\text{Se}_4\text{S}_{62}(\text{H}_2\text{CO}_2)_{18}$ and $\text{CuCd}_{65}\text{O}_4\text{S}_{62}(\text{H}_2\text{CO}_2)_{18}$ clusters in the ground singlet 1st excited triplet states. The magnitude of bond rearrangement and oxidation of the dopant is dependent on the identity of the nearest neighbors. In the example above, the inclusion of copper in a selenium matrix minimizes the effect of charge carrier-modulated dopant bonding. NB: not bonded. B: single bond, although NBO analysis consistently finds occupancy of antibonding orbitals in all cases shown above.

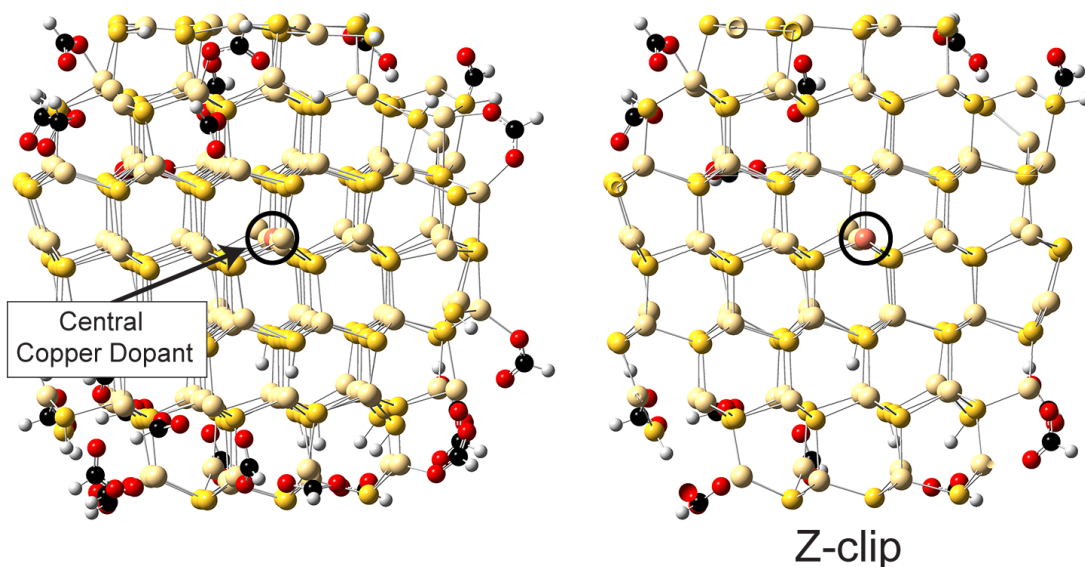


Figure S16. At the suggestion of a reviewer, shown on the left is the $\text{CuCd}_{137}\text{S}_{138}(\text{H}_2\text{CO}_2)_{25}$ cluster model and a truncated (“Z-clipped”) image on the right to highlight the central placement of a copper ion used for interior-doped DFT calculations.

References

1. Dance, I. G.; Choy, A.; Scudder, M. L. Syntheses, Properties, and Molecular and Crystal-Structures of $(\text{Me}_4\text{N})_4[\text{E}_4\text{M}_{10}(\text{SPh})_{16}]$ (E = Sulfur or Selenium; M = Zinc or Cadmium): Molecular Supertetrahedral Fragments of the Cubic Metal Chalcogenide Lattice. *J. Am. Chem. Soc.* **1984**, *106*, 6285-6295.
2. Jawaide, A. M.; Chattopadhyay, S.; Wink, D. J.; Page, L. E.; Snee, P. T. Cluster-Seeded Synthesis of Doped $\text{CdSe}:\text{Cu}_4$ Quantum Dots. *ACS Nano* **2013**, *7*, 3190-3197.
3. U.S. Environmental Protection Agency. Method 3050B: Acid Digestion of Sediments, Sludges, and Soils; 1996.
4. Bain, G. A.; Berry, J. F. Diamagnetic Corrections and Pascal's Constants. *J. Chem. Educ.* **2008**, *85*, 532.
5. Ilavsky, J.; Jemian, P. R. Irena: Tool Suite for Modeling and Analysis of Small-Angle Scattering. *J. Appl. Crystallogr.* **2009**, *42*, 347-353.